A&A 546, A75 (2012)
DOI: 10.1051/0004-6361/201219287

Astronomy & Astrophysics

Chemistry of C_3 and carbon chain molecules in DR21(OH)⋆

B. Mookerjea[1], G. E. Hassel[2], M. Gerin[3], T. Giesen[4], J. Stutzki[4], E. Herbst[5], J. H. Black[6], P. F. Goldsmith[7], K. M. Menten[8], J. Krełowski[9], M. De Luca[3], T. Csengeri[8], C. Joblin[10,11], M. Kaźmierczak[12], M. Schmidt[13] J. R. Goicoechea[14], and J. Cernicharo[14]

[1] Tata Institute of Fundamental Research, Homi Bhabha Road, 400005 Mumbai, India
e-mail: bhaswati@tifr.res.in
[2] Department of Physics and Astronomy, Siena College, Loudonville, NY 12211, USA
[3] LERMA, CNRS, Observatoire de Paris and ENS, France
[4] I. Physikalisches Institut, University of Cologne, Germany
[5] Department of Chemistry, University of Virginia, Charlottesville, VA 22904 USA
[6] Onsala Space Observatory, Chalmers University of Technology, 43992 Onsala, Sweden
[7] JPL, California Institute of Technology, Pasadena, USA
[8] MPI für Radioastronomie, Bonn, Germany
[9] Nicolaus Copernicus University, Toruń, Poland
[10] Université de Toulouse, UPS-OMP, IRAP, Toulouse, France
[11] CNRS, IRAP, 9 Av. colonel Roche, BP 44346, 31028 Toulouse Cedex 4, France
[12] SRON Netherlands Institute for Space Research, Landleven 12, 9747 AD Groningen, The Netherlands
[13] Nicolaus Copernicus Astronomical Center (CMAK), Toruń, Poland
[14] Centro de Astrobiología, CSIC-INTA, 28850 Madrid, Spain

Received 27 March 2012 / Accepted 5 August 2012

ABSTRACT

Context. C_3 is the smallest pure carbon chain detected in the dense environment of star-forming regions, although diatomic C_2 is detected in diffuse clouds. Measurement of the abundance of C_3 and the chemistry of its formation in dense star-forming regions has remained relatively unexplored.
Aims. We aim to identify the primary C_3 formation routes in dense star-forming regions following a chemical network producing species like CCH and c-C_3H_2 in the star-forming cores associated with DR21(OH), a high-mass star-forming region.
Methods. We observed velocity resolved spectra of four ro-vibrational far-infrared transitions of C_3 between the vibrational ground state and the low-energy ν_2 bending mode at frequencies between 1654–1897 GHz using HIFI on board *Herschel*, in DR21(OH). Several transitions of CCH and c-C_3H_2 were also observed with HIFI and the IRAM 30 m telescope. Rotational temperatures and column densities for all chemical species were estimated. A gas and grain warm-up model was used to obtain estimates of densities and temperatures of the envelope. The chemical network in the model was used to identify the primary C_3 forming reactions in DR21(OH).
Results. We detected C_3 in absorption in four far-infrared transitions, $P(4)$, $P(10)$, $Q(2)$, and $Q(4)$. The continuum sources MM1 and MM2 in DR21(OH), though spatially unresolved, are sufficiently separated in velocity to be identified in the C_3 spectra. All C_3 transitions are detected from the embedded source MM2 and the surrounding envelope, whereas only $Q(4)$ and $P(4)$ are detected toward the hot core MM1. The abundance of C_3 in the envelope and MM2 is $\sim 6 \times 10^{-10}$ and $\sim 3 \times 10^{-9}$, respectively. For CCH and c-C_3H_2, we only detect emission from the envelope and MM1. The observed CCH, C_3 and c-C_3H_2 abundances are most consistent with a chemical model with $n_{H_2} \sim 5 \times 10^6$ cm^{-3}, a post-warm-up dust temperature $T_{max} = 30$ K, and a time of ~ 0.7–3 Myr.
Conclusions. Post-warm-up gas phase chemistry of CH_4 released from the grain at $t \sim 0.2$ Myr and lasting for 1 Myr can explain the observed C_3 abundance in the envelope of DR21(OH), and no mechanism involving photodestruction of PAH molecules is required. The chemistry in the envelope is similar to the warm carbon chain chemistry found in lukewarm corinos. We interpret the observed lower C_3 abundance in MM1 as compared to MM2 and the envelope to be due to the destruction of C_3 in the more evolved MM1. The timescale for the chemistry derived for the envelope is consistent with the dynamical timescale of 2 Myr derived for DR21(OH) in other studies.

Key words. ISM: molecules – ISM: lines and bands – ISM: individual objects: DR21(OH) – astrochemistry – radiative transfer – molecular data

1. Introduction

Small carbon chains are important for the chemistry of stellar and interstellar environments for several reasons: they are ubiquitous throughout the interstellar medium (Ádámkovics et al. 2003), they are likely to participate in the formation of long carbon chain molecules, and they are products of photofragmentation cascades of polycyclic aromatic hydrocarbons (PAHs; Radi et al. 1988; Pety et al. 2005). Triatomic carbon, C_3, was first tentatively identified in interstellar gas by Van Orden et al. (1995) and Haffner & Meyer (1995). The mid-infrared spectrum of C_3 (ν_3 antisymmetric stretching mode) was measured in the circumstellar envelope of CW Leo (IRC +10216) by Hinkle et al. (1988), and in low-resolution interstellar absorption in the far-IR (ν_2 bending mode) toward the Sgr B2 star-forming

⋆ *Herschel* is an ESA space observatory with science instruments provided by European-led Principal Investigator consortia, with important participation from NASA.

Table 1. Properties of the sources in DR21(OH).

Component	α(2000)	β(2000)	v_{LSR} (km s^{-1})	Mass[a] ($M_\odot$)	T_d	$N(H_2)$[b] (10^{23}cm^{-2})	$\langle n(H_2)\rangle$ (10^7 cm^{-3})	References
MM1	$20^h39^m01\overset{s}{.}0$	$42°22'48''$	-4.1 ± 0.3	88	58	4.5	4.1	1, 2
MM2	$20^h39^m00\overset{s}{.}4$	$42°22'43\overset{''}{.}8$	-0.7 ± 0.3	143	30	7.4	6.8	1, 2
Envelope	...	...	-3.1 ± 0.3	118[c]		3.5	0.3	1, 3, 4

Notes. [(a)] All estimated for a distance of 1.5 kpc. [(b)] Within a 15″ beam. [(c)] Mass of the envelope derived by removing the contributions of MM1 and MM2 from the total mass of the region estimated by Motte et al. (2007).

References. (1) Mangum et al. (1991); (2) Mangum et al. (1992); (3) Wilson & Mauersberger (1990); (4) Motte et al. (2007).

region and IRC+10216 by Cernicharo et al. (2000). Giesen et al. (2001) discussed new laboratory data on the vibrational spectrum of C_3 in its low-frequency bending mode and revisited the first identification of the ν_2 $R(2)$ line in absorption toward Sgr B2 (Van Orden et al. 1995). The abundance and excitation of C_3 with a large range of rotational temperatures in translucent clouds have also been determined convincingly (Maier et al. 2001; Roueff et al. 2002; Oka et al. 2003; Ádámkovics et al. 2003) through observations at optical wavelengths. In addition, Galazutdinov et al. (2002) demonstrated that the C_3 abundance is related neither to interstellar reddening nor to the intensities of diffuse interstellar bands.

DR21(OH) lies 2′ north of the H II region DR21, in the Cygnus X H II complex. The distance to DR21(OH) has recently been accurately determined by trigonometric parallax measurements of its associated methanol masers as $1.50^{+0.08}_{-0.07}$ kpc (Rygl et al. 2012). Interferometric and high-resolution single-dish observations both in continuum and molecular lines have shown multiple peaks in DR21(OH) (Wilson & Mauersberger 1990; Mangum et al. 1991, 1992; Chandler et al. 1993). Mangum et al. (1992) resolved the main DR21(OH) peak into two sources, MM1 and MM2, and MM2 into two subsources, MM2-A and MM2-B. Synthesis imaging of NH_3 emission from the region has clearly resolved MM1 and MM2, which have radial velocities -4.1 ± 0.3 km s^{-1} and -0.7 ± 0.3 km s^{-1}, respectively (Mangum et al. 1992). Both star-forming cores MM1 and MM2 in DR21(OH) are young, with no visible H II region and only very weak continuum emission at the centimeter wavelengths (Argon et al. 2000). Dust continuum observations suggest that MM1 is the brighter source ($L = 1.7 \times 10^4$ $L_\odot$; ZAMS B0V star) and shows evidence of star formation, whereas MM2 ($L = 1.2 \times 10^3$ $L_\odot$; early B star), though more massive, is fainter and most likely at an earlier stage of evolution. The region is characterized as a high-mass star-forming region due to the detection of centimeter and millimeter maser emission from numerous transitions, e.g., H_2O, OH and CH_3OH (Araya et al. 2009; Fish et al. 2005; Mangum et al. 1992; Plambeck & Menten 1990). MM1 also contains ground-state OH masers at 1.6 GHz and 6.7 GHz class II CH_3OH masers near the peak of the dust and centimeter continuum emission (Argon et al. 2000; Fish et al. 2005; Rygl et al. 2012). In a recent interferometric study of the continuum emission at 1.4 mm from DR21(OH), Zapata et al. (2012) have resolved MM1 and MM2 into nine compact sources. Five of the compact sources are associated with MM1 and four with MM2. Two of the compact sources associated with MM1 (SMA6 and SMA7) seem to show hot core activity. White et al. (2010) have observed multiple transitions of CO from 4–3 to 13–12 using *Herschel*/SPIRE to conclude the presence of two components at 80 K and 180 K from a rotation temperature analysis. From an LVG analysis, these authors obtain $T_{kin} = 125$ K and $n_{H_2} = 7 \times 10^4$ cm^{-3}. We summarize selected properties of all emission components in DR21(OH) as available from the literature in Table 1. All values in Table 1 correspond to a distance of 1.5 kpc.

With its broad frequency coverage, high sensitivity, and spectral resolution, the Heterodyne Instrument for the Far-Infrared (HIFI; de Graauw et al. 2010) on board the *Herschel* Space Observatory (Pilbratt et al. 2010), has provided for the first time the opportunity for a systematic study of carbon chain molecules such as C_3 through probing several ro-vibrational lines at full spectral resolution. The results presented here are a part of the PRISMAS "PRobing InterStellar Molecules with Absorption line Studies" key program (Gerin et al. 2010).

The primary aim of the paper is to understand the C_3 formation mechanism. Observations of diffuse interstellar gas at optical and IR wavelengths have shown a strong correlation between the column densities of C_3 and C_2. This suggests that C_3 and C_2 are in the same chain of chemical reactions (Oka et al. 2003). The formation routes for C_3 starting from C_2 also involved the production of CCH and c-C_3H_2. However, no transitions of C_2 are available at longer wavelengths (far-infrared and longer), which can be used to detect C_2 in dense star-forming regions, where C_3 is detected in absorption (Mookerjea et al. 2010). Thus, to understand the formation pathway of C_3, we compare the abundances of C_3, CCH, and c-C_3H_2, with results of chemical models of dense star-forming cores.

2. Observations

2.1. Herschel data: C_3 and CCH

We observed in DR21(OH) four lines of the ν_2 fundamental band ($P(4)$, $Q(2)$, $Q(4)$ and $P(10)$), of triatomic carbon using the upper sideband of the HIFI bands 7a and 7b as well as the lower sideband of band 6b of the HIFI receiver. All C_3 spectra were observed at a single position in DR21(OH) with coordinates α(J2000) = 20:39:01.00 δ(J2000) = 42:22:48.0, in the dual beam switch mode. The observations were carried out on 2010 June 25 and November 25 to 27. The details of the observations and data reduction are given in Mookerjea et al. (2010). All spectra were smoothed to resolution between ~0.16 to 0.18 km s^{-1}, and the rms noise level for the spectra is 0.03 to 0.04 K. All the observed C_3 lines are at frequencies for which HEB mixers are used in HIFI, and we noticed a variation in the level of the continuum observed for different LO settings and polarizations for a particular spectral line. In the results presented here, there is only a shift in the continuum level, with little or no change in the depth of absorption. We verified that this shift in the continuum level does not arise from differences in the pointing of the telescope or the notorious HEB-band standing waves. We find the uncertainty in the continuum level to be most pronounced

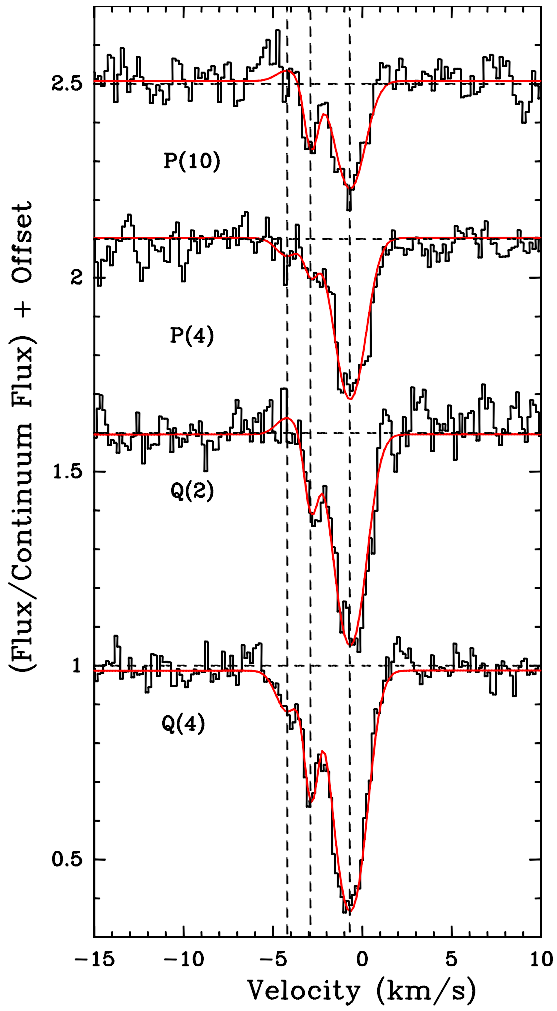

Fig. 1. HIFI observations of the C_3 lines in DR21(OH). The spectra are corrected for the DSB continuum and normalized to the SSB continuum level. The $Q(2)$, $P(4)$, and $P(10)$ spectra are shifted consecutively by +0.5, so that the plots do not overlap. The red line shows the simultaneous fit with three Gaussian velocity components (at −0.7, −2.9, and −4.2 km s^{-1}). Note that the third component is only detected above the noise in $Q(4)$ and $P(4)$. The "negative" absorption bumps at this velocity fitted in $Q(2)$ and $P(10)$ are within the noise.

for the $P(4)$ line at 1787 GHz. We evaluated the effect of these variations and included them in our estimate of uncertainties of the column densities (Sect. 3.1).

Figure 1 shows the observed spectra normalized to the (single sideband) continuum level. The observed C_3 absorption features occur around the systemic velocity (∼−1 km s^{-1}) of an infalling subfilament on DR21(OH) (see Schneider et al. 2010) and hence are associated with the source only and not with foreground material. The PRISMAS observations are not sensitive enough to detect C_3 lines in absorption in the diffuse gas along the line of sight to DR21(OH) (Mookerjea et al. 2010).

As part of the PRISMAS program, a large number of emission lines falling within the multiple observed bands were found, in addition to the target lines detected in absorption towards DR21(OH).

Here we use the two spectral lines of CCH at 523.97 and 524.03 GHz in DR21(OH) in HIFI Band 1a.

Table 2 summarizes the spectroscopic parameters of the species and transitions observed with *Herschel*.

2.2. IRAM 30 m data: CCH and c-C_3H_2

The ground state transition of CCH at 87.316 GHz (N = 1–0, J = 3/2–1/2, with three hyperfine components) and the $2_{1,2}$–$1_{0,1}$ transition of c-C_3H_2 at 85.338 GHz were observed by Gerin et al. (2011) using the IRAM-30 m telescope in 2006, August and December. Table 3 presents both spectroscopic and observational parameters of the lines observed with IRAM 30 m. The primary aim of these observations was the study of CCH and c-C_3H_2 in the diffuse and translucent clouds along the line of sight to DR21(OH). However, as do the HIFI data, these observations also detect the emission lines arising from the source DR21(OH) itself.

2.3. Position of beams relative to the continuum sources in DR21(OH)

Figure 2 presents the 12″ (C_3) and 43″ (CCH at 522 GHz) beams of HIFI and the 29″ IRAM 30 m beams overlaid on the images of 3 mm and 450 μm continuum emission from DR21(OH). The 3 mm continuum emission (color and black contours) was observed with PdBI (Csengeri et al. 2011), and the 450 μm (yellow contour) continuum data were obtained from the JCMT archives. We see that the 3 mm interferometric map (restored to a beam of 2″) clearly resolves the continuum sources MM1 and MM2 and also shows evidence for extended emission from the envelope. At a resolution of 8″, the 450 μm JCMT data shows that the continuum emission is primarily dominated by the surrounding extended envelope. The C_3 beam of HIFI covers a significant part of the source MM2 as well. The 29″ IRAM 30 m beam almost completely covers the larger region sampled by the 522 GHz HIFI beam. Thus, Fig. 2 shows that the observing beams for all the spectral observations presented in this paper cover regions including MM1, MM2, and the surrounding envelope. The spectral indices of the continuum emission derived so far from the 3 mm (PdBI) and 1.4 mm (SMA Zapata et al. 2012) data are not consistent with thermal emission from dust. It is thus difficult to characterize the contribution of MM1 and MM2 to the continuum emission. However, at the beam sizes of our C_3 observations at THz frequencies, it is probable that the continuum is dominated by the emission from the extended envelope and hence variation due to the contribution of the individual sources is likely to be small. We thus assume that all the C_3 absorption is of the same continuum, produced primarily from the extended envelope.

3. Results

3.1. C_3 column densities

The observed C_3 absorption spectra show evidence of multiple velocity components (Fig. 1). The $Q(4)$ transition clearly shows three velocity components, while the other transitions distinctly show two components. In a global fitting scheme, we assumed that each C_3 transition has contributions from three velocity components and then fitted all observed transitions simultaneously using multi-component Gaussians. The parameters fitted simultaneously in each transition are the common v_{LSR}, Δv for each of the three velocity components and the strength of the absorption dips, separately for each line. We thus assumed all three velocity components to be present in all transitions, even if the components are not explicitly seen, since we attribute the non-detection to the lower strength of the transition relative to the achieved rms of our observations rather than to any physical

Table 2. Spectroscopic parameters for the C_3 and CCH transitions observed with *Herschel*/HIFI.

Species	Transition	Frequency (MHz)	A-coeff (s^{-1})	E_l (cm^{-1})	Beam size
C_3, (J, v)	(9, 1)–(10, 0) P(10)	1 654 081.66	2.38×10^{-3}	47.3	13″
	(3, 1)–(4, 0) P(4)	1 787 890.57	2.72×10^{-3}	8.6	12″
	(2, 1)–(2, 0) Q(2)	1 890 558.06	7.51×10^{-3}	2.6	11″
	(4, 1)–(4, 0) Q(4)	1 896 706.56	7.58×10^{-3}	8.6	11″
CCH, $N_{J,F}$	$6_{13/2,7}$–$5_{11/2,6}$	523 971.5704	4.58×10^{-4}	43	40″
	$6_{13/2,6}$–$5_{11/2,5}$	523 972.1630	4.53×10^{-4}	43	40″
CCH, $N_{J,F}$	$6_{11/2,6}$–$5_{11/2,5}$	524 033.9075	4.51×10^{-4}	43	40″
	$6_{11/2,5}$–$5_{9/2,4}$	524 034.5305	4.43×10^{-4}	43	40″

Notes. [(*)] *Herschel*/HIFI beam sizes are taken from Roelfsema et al. (2012).

Table 3. Spectroscopic and observational parameters for the transitions of CCH and c-C_3H_2 observed with IRAM 30 m.

Species	Transition	Frequency (MHz)	A-coeff (s^{-1})	E_l (cm^{-1})	θ_{FWHM} (″)	F_{eff}[a]	B_{eff}[b]
CCH, $N_{J,F}$	$1_{3/2,1}$–$0_{1/2,1}$	87 284.1050	2.60×10^{-7}	0.0015	29″	0.95	0.75
	$1_{3/2,2}$–$0_{1/2,1}$	87 316.8980	1.53×10^{-6}	0.0015	29″	0.95	0.75
	$1_{3/2,1}$–$0_{1/2,0}$	87 328.5850	1.27×10^{-6}	0.0015	29″	0.95	0.75
c-C_3H_2, (J_{Ka}, K_c)	$2_{1,2}$–$1_{0,1}$	85 338.8930	2.32×10^{-5}	1.7	29″	0.95	0.75

Notes. [(a)] F_{eff} forward efficiency and [(b)] B_{eff} beam efficiency of the telescope.

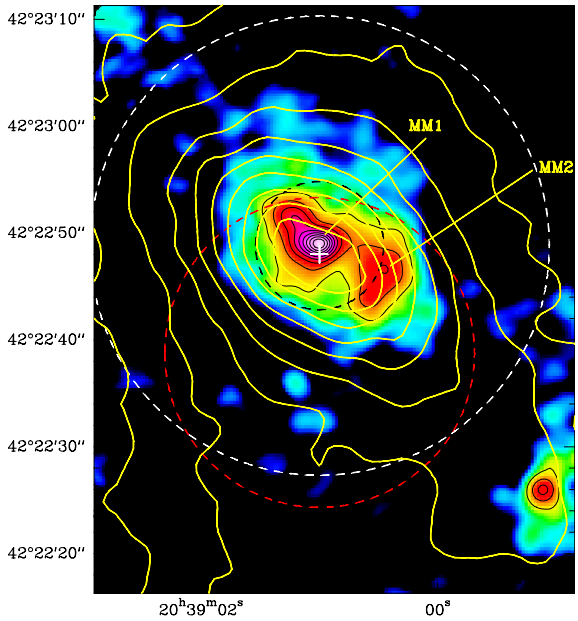

Fig. 2. The 3 mm PdBI continuum image of DR21(OH) in color and black contours overlaid with yellow contours of 450 μm image observed with JCMT SCUBA. Also overlaid on the continuum image are the FWHM beam sizes for spectroscopic observations. The dashed lines show the HIFI (12″, black, and 43″, white) and IRAM 30 m (29″, red) beams. The white cross denotes the center of the HIFI beams.

or chemical reason. All four spectra show evidence of two major velocity components centered at $v_{LSR} = -2.85 \pm 0.04$ km s^{-1} and $v_{LSR} = -0.68 \pm 0.02$ km s^{-1}, with the latter component being stronger. The third velocity component detected only in $Q(4)$ and marginally in the $P(4)$ spectra is at -4.2 ± 0.2 km s^{-1}. We checked that for a particular transition in which the third component is undetected the results of fitting do not change significantly for the well-detected velocity components assuming the presence of the third component. Table 4 presents the single sideband continuum levels (estimated from double sideband temperatures assuming a sideband gain ratio of 1) and the results of the Gaussian fit along with their uncertainties.

We compare the velocity components at -0.7, -2.9 km s^{-1}, and -4.2 km s^{-1} with the known velocities in the region. The LSR velocities of the sources MM1 and MM2 are -4.1 and -0.7 km s^{-1}, respectively, and the peak of $C^{18}O$ emission is observed to have a v_{LSR} of -3.2 km s^{-1} at a resolution of 12″, which most likely arises from the envelope surrounding MM1 and MM2 (Mangum et al. 1992; Wilson & Mauersberger 1990). Our observation is centered on MM1; MM2, located 8.″3 away from MM1, lies within the HIFI beam. Thus, although we cannot resolve MM1 and MM2 spatially, the velocities of the two sources and the envelope differ sufficiently from one another to allow identification of the three components in the C_3 spectra. We detect C_3 absorption due to MM2 and the envelope in all transitions, while MM1 appears only in the stronger $Q(4)$ transition and marginally in $P(4)$ transition. Based on the $J = 4$ column densities derived for the -4.2 km s^{-1} component assuming T_{rot} between 50–70 K, we estimate the expected absorption depths for the $J = 2$ level to be only 10% and even less for the $J = 10$ level; this is comparable to the uncertainty in our measurements. Thus, the nondetection of the -4.2 km s^{-1} component in $Q(2)$ and $P(10)$ is consistent with the expected strengths of these lines.

Taking into consideration the uncertainties in the measurements described above, we estimate the state-specific column densities to be $\sim 10^{14}$ cm^{-2} and $\sim 10^{13}$ cm^{-2} for the -0.7 km s^{-1} and -2.9 km s^{-1} components, respectively (Table 4). For $Q(4)$ and $P(4)$, and the additional absorption feature at -4.2 km s^{-1} corresponds to a $J = 4$ column density of $\sim 10^{13}$ cm^{-2}. Given the marginal detection at $P(4)$ and nondetection at $Q(2)$, we propose the $J = 4$ column density for the -4.2 km s^{-1} component to be an upper limit. Using the $J = 2$, 4, and 10 levels, we construct rotation diagrams and obtain rotation temperatures

Table 4. Single sideband continuum antenna temperatures (T_c) and parameters derived from simultaneous Gaussian fitting of all the line profiles and the lower state C_3 column densities (N_l) estimated from the fitted intensities.

Transition	T_c [K]	V_{cen} [km s^{-1}]	$\int \tau dv$ [km s^{-1}]	N_l [10^{14} cm^{-2}]
$P(10)$	7.1 ± 0.4	−0.7	0.60 ± 0.07	1.2 ± 0.08
		−2.9	0.17 ± 0.04	0.3 ± 0.06
		−4.2	...	...
$P(4)$	7.0 ± 1.3	−0.7	1.00 ± 0.06	2.5 ± 0.1
		−2.9	0.08 ± 0.03	0.2 ± 0.07
		−4.2	0.07 ± 0.03	0.17 ± 0.08
$Q(2)$	$7.1^{+0.6}_{-0.5}$	−0.7	1.46 ± 0.05	1.2 ± 0.06
		−2.9	0.19 ± 0.03	0.2 ± 0.04
		−4.2	...	...
$Q(4)$	$6.7^{+0.3}_{-0.7}$	−0.7	1.79 ± 0.04	1.5 ± 0.06
		−2.9	0.33 ± 0.03	0.3 ± 0.03
		−4.2	0.16 ± 0.03	0.1 ± 0.06
Total[a]		−0.7	...	9.1 ± 2.3
		−2.9	...	2.2 ± 0.4

Notes. The error bars in N_l include errors due to both uncertainty in the continuum level and the line-fitting procedure. The velocity components are as follows: component 1: $v_{cen} = -0.68 \pm 0.02$ km s^{-1}, $\Delta V = 1.85 \pm 0.51$ km s^{-1}, component 2: $v_{cen} = -2.85 \pm 0.04$ km s^{-1}, $\Delta V = 0.86 \pm 0.08$ km s^{-1}, and component 3: $v_{cen} = -4.2 \pm 0.2$ km s^{-1}, $\Delta V = 1.4 \pm 0.4$ km s^{-1}. Velocity component 3 is detected only above the noise level in $P(4)$ and $Q(4)$. [(a)] Estimated using rotation diagram (Fig. 3).

of 76 ± 20 K and 48 ± 6 K for the velocity components at −2.9 km s^{-1} and −0.7 km s^{-1}, respectively (Fig. 3). The total C_3 column densities for the −2.9 km s^{-1} and −0.7 km s^{-1} components are $(2.2 \pm 0.4) \times 10^{14}$ cm^{-2} and $(9.1 \pm 2.3) \times 10^{14}$ cm^{-2}, respectively. Thus, the −0.7 km s^{-1} component corresponds to the colder and higher column density gas.

3.2. CCH column densities

In the PRISMAS observations we detected five transitions of CCH at frequencies around 87.3 GHz and 524.0 GHz. We first attempted to derive a self-consistent LTE model, which explains the intensities of all the CCH transitions using a combination of XCLASS (Schilke et al. 1999; Comito et al. 2005) and MAGIX (Bernst et al. 2011). XCLASS generates synthetic spectra consisting of multiple velocity components as well as hyperfine structure components for all transitions of different chemical species. XCLASS accesses the molecular databases CDMS and JPL and models each molecule with the following free parameters: source size, temperature, column density, line width and velocity offset relative to the systemic velocity of the source. It also derives the column density corresponding to the different velocity components detected in absorption and emission in the observed spectra. The source size refers to the size of the cloud contributing to the emission or absorption spectra. The synthetic spectra generated with XCLASS were fitted to the observed spectra using MAGIX, an iterating engine that allows automatic minimization to constrain model parameters. We assumed that the hyperfine lines have the same excitation temperatures. We note that the fitting procedure can involve considerable degeneracy between source size, excitation temperature and column

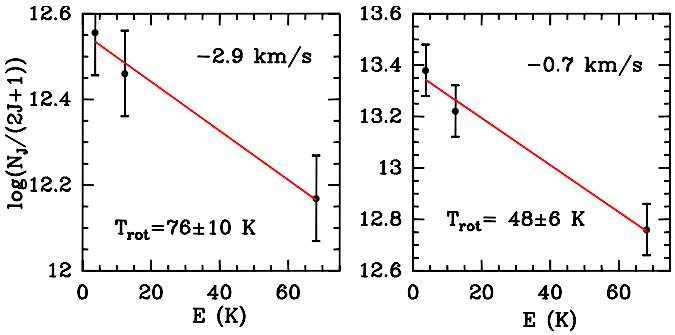

Fig. 3. Rotation diagram of C_3 for the velocity components at −0.7 km s^{-1} and −2.9 km s^{-1}. The errorbars correspond to an estimated error of 10% in the state specific column densities and are conservative estimates, which include uncertainties due to continuum measurements as well as the noise in the spectra.

density. In the absence of more accurate information, we fixed the source sizes for MM1 and MM2 to 15″ and the size for the envelope to 30″. Using XCLASS/MAGIX we could not obtain an LTE model that consistently explained the intensities of all five lines of CCH. We found that the 87 GHz lines have intensities much higher than the expected values based on the 524 GHz intensities under the assumption of LTE. We thus fitted two different LTE models to the 87 GHz and 524 GHz spectra of CCH. Figures 4a and b show the observed CCH spectra along with the LTE models fitted using XCLASS; the fit parameters are presented in Table 5. The errorbars for the parameters in Table 5 represent the range of values over which the best-fit model does not change significantly.

From the intensities of the 87.316 GHz CCH lines, we estimate the LTE temperatures of the −0.5, −2.9, and −4.2 km s^{-1} components contributing to the CCH emission to be 110 K, 9 K, and 111 K, respectively. The CCH transition at 524 GHz shows evidence of only two velocity components at −2.8 km s^{-1} and −4.6 km s^{-1}, with temperatures of 33 K and 101 K respectively.

While the temperatures of the envelope derived from the LTE models of the 87 GHz and the 524 GHz transitions are not too discrepant, the total CCH column densities of the envelope ($v_{cen} = -2.7$ km s^{-1}) estimated from the two transitions are 2.3×10^{15} cm^{-2} and 2.9×10^{14} cm^{-2}, respectively, hence differing by a factor ∼8. This discrepancy in column densities indicates two possibilities. First, it is likely that the excitation of CCH is non-LTE, so while the 87 GHz transition with a low critical density is thermalized and traces the total column density better, a commensurate number of molecules in the higher energy levels probed by the 524 GHz lines are not present. Second, owing to the difference in the pointing centers of the beams the 87 GHz data could also be tracing the emission from the extended ridge in DR21(OH), whereas the higher-J lines at 524 GHz primarily trace the DR21(OH) hot core and the envelope. Though difficult to quantify, the difference in coupling of the emission with the beams at 87 and 524 GHz, which are of different sizes and differently centered, could contribute to part of the discrepancy. For consistent comparison of the abundances of CCH, c-C_3H_2 and C_3 in the envelope, we use the column densities derived from the 87 GHz CCH transitions as an upper limit for chemical models discussed later.

3.3. LTE modeling of c-C_3H_2

We also derived an LTE model for the single c-C_3H_2 line using a two-component Gaussian profile corresponding to the velocities

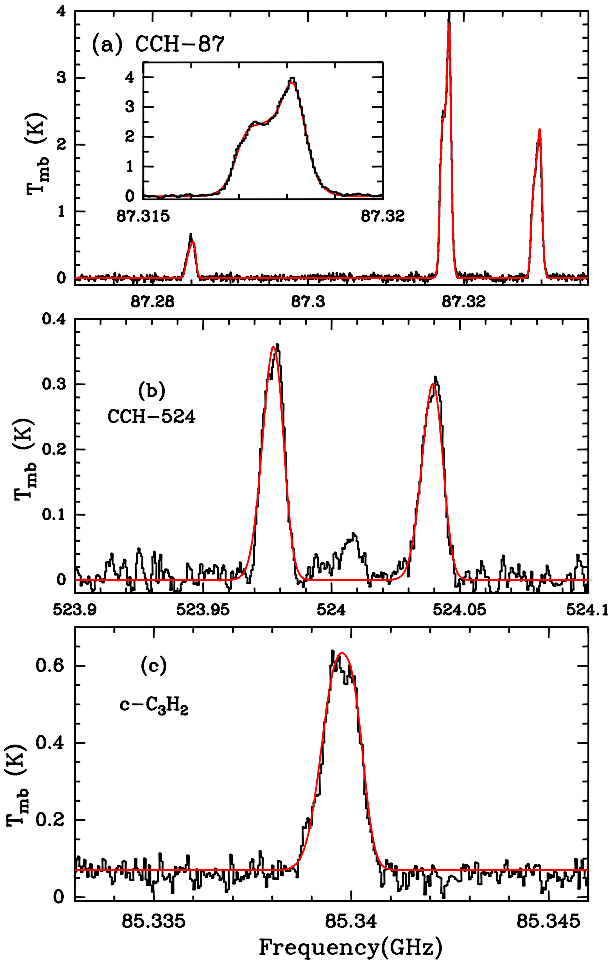

Fig. 4. Spectra of **a)** CCH at 87.316 GHz, **b)** CCH at 523.9 GHz, and **c)** C_3H_2 at 85.338 GHz fitted with LTE models using XCLASS. The spectra of (a) also show the main hyperfine component of 87.316 GHz as inset to demonstrate the velocity structure better.

Table 5. Parameters derived from fitting the CCH (observed with HIFI and IRAM) and c-C_3H_2 lines with LTE models using XCLASS.

Species	Size	T	N	Δv	v_{LSR}
	$''$	K	10^{14} cm^{-2}	km s^{-1}	km s^{-1}
CCH-87	15	110 ± 15	19.7 ± 3.0	1.6 ± 0.1	−0.6 ± 0.1
	30	9 ± 2	23.4 ± 1.3	3.5 ± 0.1	−2.7 ± 0.1
	15	111 ± 10	60.3 ± 4.0	1.7 ± 0.1	−4.2 ± 0.1
CCH-524	30	33 ± 5	1.2 ± 0.3	5.5 ± 0.2	−2.8 ± 0.2
	15	101 ± 11	1.4 ± 0.3	4.5 ± 0.2	−4.6 ± 0.2
C_3H_2	30	31 ± 4	0.7 ± 0.1	3.3 ± 0.1	−2.7 ± 0.1
	15	78 ± 6	0.9 ± 0.2	1.5 ± 0.2	−4.5 ± 0.2

Notes. Parameters without errorbars were held constant for the fitting.

around −2.7 km s^{-1} and −4.5 km s^{-1}. Figure 4c shows the observed c-C_3H_2 spectrum fitted with a two-component model using XCLASS.

3.4. Temperature structure in DR21(OH)

Based on the results of synthesis imaging of thermal NH_3 and detection of the (7, 7) transition of NH_3, which is 535 K above the ground state, the kinetic temperature of the gas associated with MM1 (v_{LSR} = −4.1 km s^{-1}) is estimated to be >80 K (Mangum et al. 1992; Mauersberger et al. 1986). Wilson & Mauersberger (1990) derived a kinetic temperature of 34 K for this region using NH_3 observations at a resolution of 40″.

We note that the 43″ beam size for the 524 GHz HIFI observations and the 29″ beam size of IRAM 30 m (Fig. 2) include MM1, MM2, and the envelope. Hence, the observed CCH emission is primarily due to the molecular gas surrounding all these sources, which is traced in CO and $C^{18}O$. Using CCH and c-C_3H_2, we derive the temperature of the component corresponding to the envelope to be 10–30 K and the temperature of the component associated with MM1 to be 100–110 K. The data on carbon chain molecules are consistent with the presence of high temperatures in MM1 and MM2 and agree with the previous determinations.

Table 6. Comparison of observed abundances of the chemical species in the envelope of DR21(OH) and other sources.

Species	DR21(OH)		Lukewarm corino[b]	Hot corino[c]
	N	X^a	X	X
	cm^{-2}	×10^{-9}	×10^{-9}	×10^{-9}
C_3	2.2×10^{14}	0.63	...	...
CCH (87 GHz)	2.3×10^{15}	6.6	(5.3–12.8)	0.05
CCH (524 GHz)	2.9×10^{14}	0.8	(5.3–12.8)	0.05
c-C_3H_2	6.8×10^{13}	0.19	0.22	...[d]

Notes. [(a)] Estimated using $N(H_2) = 3.5 \times 10^{23}$ cm^{-2} (Table 1). [(b)] Sakai et al. (2009a,b). [(c)] Sakai et al. (2009a); Cazaux et al. (2003); Bisschop et al. (2007). [(d)] Observations not available, Hassel et al. (2011) model ($n_{H_2} = 5 \times 10^5$ cm^{-3}) predicts X(c-C_3H_2) ≈ 10^{-9} in lukewarm corinos ($T \sim 30$ K) and X(c-C_3H_2) ≈ 10^{-7} in hot cores ($T \sim 100$ K).

4. Modeling observed chemical abundances in the envelope

4.1. The OSU gas-grain models

We model the observed abundances of the three chemical species C_3, c-C_3H_2, and CCH (Table 6) in the warm envelope around DR21(OH) using the Ohio State University (OSU) gas-grain code with a warm-up (Hasegawa et al. 1992; Garrod & Herbst 2006). Although slightly shifted in velocity from the envelope at −4.2 km s^{-1} detected in C_3 for CCH-524 and c-C_3H_2, we consider the −4.5 km s^{-1} velocity component to correspond to the envelope. Since the models are primarily for dense star-forming regions and the low-frequency CCH transition (87 GHz) likely traces an additional extended component, we use the CCH abundance derived from the IRAM data as an upper limit to compare with the outcome of the model. Motte et al. (2007) estimated the average volume density of the entire region to be 10^6 cm^{-3}, while the MM1 and MM2 dense cores reach densities larger than 10^7 cm^{-3} (Table 1). Thus, for the envelope we presently consider models with constant gas densities $n_{H_2} = 5 \times 10^5$, 1×10^6, and 5×10^6 cm^{-3}.

The gas-grain network considers 7166 reactions involving a total of 668 gaseous and surface species, where the surface species are identified with (s). The physical parameters and initial chemical abundances adopted are the same as used by

Table 7. Parameters for the models explored for C_3 chemistry in DR21(OH).

Model	T_{max} (K)	n_{H_2} (cm^{-3})
1	30	5×10^5
2	30	1×10^6
3	30	5×10^6
4	50	5×10^5
5	50	1×10^6
6	50	5×10^6

Table 8. Parameters assumed to remain constant in present models.

Parameter	Value	Unit
[b] Cosmic Ray Ionization Rate ζ	1.3×10^{-17}	s^{-1}
[b] Visual Extinction A_V	10	
[a,b] Grain Radius a_d	1×10^{-5}	cm
[a,b] Nonthermal Desorption Yield a_{RRK}	0.01	
[a,b] Initial Temperature T_i	10	K
[a,b] Warm-up Timescale t_{sc} [a,b]	2×10^5	yr
[b] Warm-up Offset Time t_{off}	1×10^5	yr

Notes. [(a)] Garrod & Herbst (2006); [(b)] Hassel et al. (2008).

Garrod et al. (2007) and Hassel et al. (2008, Tables 1 and 2). In this approach, a one-point parcel of material undergoes an initially cold period of $T_0 = 10$ K with a duration of $t = 10^5$ yr, followed by a gradual temperature increase. A heating timescale of $t_h = 0.2$ Myr is adopted following Garrod & Herbst (2006), where we use values for the maximum temperature T_{max} of 30 K and 50 K, so that the model reaches T_{max} by $t \approx 0.3$ Myr. A total of six combinations of T_{max} and n_{H_2} are considered, as outlined in Table 7. In contrast to more complex hydrodynamic approaches (Aikawa et al. 2008), the other physical parameters here (Table 8) are assumed to be homogeneous at any given time and from one model to another. The advantage of this approach is that it allows a more detailed look at the chemical processes and the roles of individual reactions. A similar procedure was previously used to simulate the formation of hydrocarbon chains in the envelopes of low-mass protostellar envelopes by Hassel et al. (2008) and Hassel et al. (2011), where the latter model also considered the linear C_3 detected toward W31C and W49N (Mookerjea et al. 2010).

The models include photodesorption rates for CO(s), N_2(s), H_2O(s), and CO_2(s) based on the measurements of Öberg et al. (2007, 2009a,b). The adopted processes and rates are species-dependent, rather than dependent on a single parameter.

The production of hydrocarbon chains during the warm-up has been attributed to a process beginning with grain surface chemistry. The elevated temperature allows methane to evaporate from the ice mantles surrounding dust particles and act as a precursor for a carbon-chain rich ion-molecule chemistry. Hassel et al. (2011, Fig. 6) demonstrated that the abundance of C_3 is subject to such a process. In particular, the C_3 is formed via gas phase chemistry involving atomic C at early times and depletes sharply at $t \sim 10^5$ yr, after which time most available atomic C is incorporated into CO. In the absence of grain surface chemistry, the C_3 will continue to deplete to abundances below 10^{-12} by 1 Myr. In models including grain surface chemistry, the abundance of C_3 is regenerated following the release of CH_4(s) and subsequent gas phase chemistry during the warm-up. The abundances and reactions discussed in this section refer to the gas phase.

4.2. Model results

The time evolution of fractional abundances is presented for C_3, CCH and c-C_3H_2 in Fig. 5, along with the corresponding observed values. In all models, the warm-up occurs between 0.1 and 0.3 Myr starting from an initial temperature of 10 K, similar to the temperature profiles that appear in Hassel et al. (2008, Figs. 2 and 3). We observe the following general trends in the abundance profiles shown in Fig. 5: for the lower temperature models (1–3), the molecular abundances attain values comparable to the observed abundances for a much longer period of time as compared to the higher temperature models (4–6). Further, for both C_3 and c-C_3H_2 in models 4–6, the maximum abundance decreases with increasing values of n_{H_2}.

Figure 5 shows that all six models produce CCH to a peak abundance of $X = 0.2\text{–}1 \times 10^{-8}$ during the warm-up. The abundance depletes more rapidly for models 4–6, while the abundance remains elevated for a longer period for models 1–3. Moreover, higher densities produce a slightly smaller CCH abundance following the warm-up. The C_3 abundance depletes more rapidly for models 4–6, and smaller abundances are produced for larger density during this period. All the models produce a similar abundance of c-C_3H_2 in the range of $X = 0.5\text{–}1 \times 10^{-8}$ following the warm-up. The temperature and density effects seen in the previous two species also appear for c-C_3H_2 but to a lesser extent.

The primary reason for the difference in abundance of the chemical species considered here for $T_{max} = 30$ K and 50 K models is that the higher temperature will release additional species from the icy grain mantles to the gas. This leads to additional, competitive reaction pathways with the overall effect of a comparative depletion of abundance of these particular species. A similar effect is visible at the onset of the warm-up, when the abundances of the three species deplete sharply just prior to the steep increase attributed to the warm-up.

4.3. Major chemical reactions

Table 9 summarizes the most important chemical reactions occurring in the gas phase during warm-up as determined by the gas-grain chemistry model (Garrod & Herbst 2006). We emphasize that the species produced here also result from other ion-molecule reactions and that Table 9 lists only the most direct and salient mechanisms. The liberated CH_4 reacts with C^+ to form the intermediate species $C_2H_2^+$ and $C_2H_3^+$ via reactions (1) and (3). Subsequently, the reaction of H_2 with $C_2H_2^+$ in (2) produces $C_2H_4^+$. The dissociative recombination reaction of an electron with these intermediate ions then produces C_2H_2 by reaction (2) or reaction (5). Further reactions of CH_4 with the intermediate ions can produce $C_3H_5^+$ via reactions (6) and (7), while the dissociative recombination of $C_3H_5^+$ produces C_3H_3 via reaction (8). Reactions of C and C^+ with C_2H_2 (9, 11) produce C_3H and C_3H^+. Further reaction of these products (12, 13) produce $C_3H_2^+$, and the reaction of CH_4 with $C_3H_2^+$ (14) produces $C_3H_3^+$. The C^+ and C result from partial desorption of CO(s) and subsequent reaction with He^+ during the warm-up. These represent the major precursors for the observed species and provide the basis to examine each species individually.

For the chemical species considered here, we identify the primary formation reactions as follows: CCH is primarily formed by the dissociative recombination of $C_2H_3^+$ in reaction (17). The evolution of C_3 proceeds in a somewhat different manner.

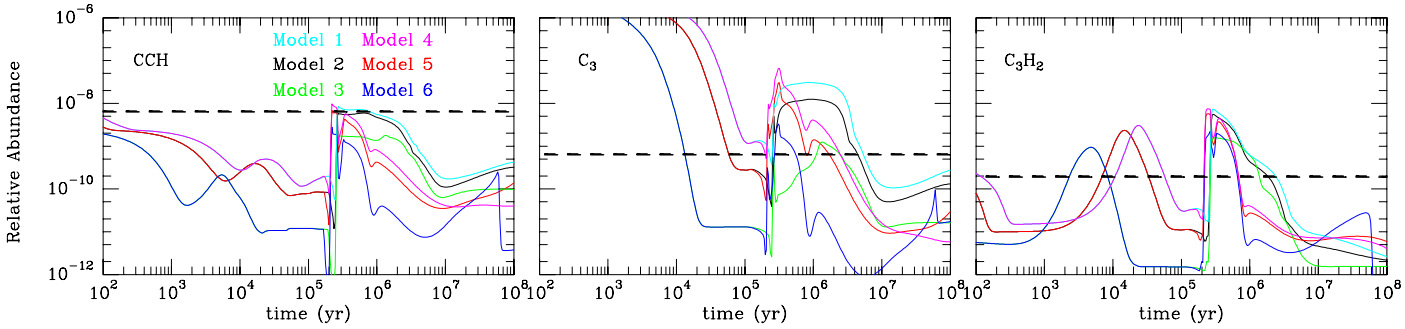

Fig. 5. Comparison of observed abundances in the envelope (shown by dashed lines) with the results of chemical models involving warming up of grains for different combinations of hydrogen density (n_{H_2}) and final warm-up temperatures. The model calculates abundances relative to hydrogen, and the observed column densities of the different species have been converted to fractional abundances assuming $N(H_2) = 3.5 \times 10^{23}$ cm^{-2}. In all models, the warm-up occurs between 0.1 and 0.3 Myr starting from an initial temperature of 10 K, similar to the temperature profiles that appear in Hassel et al. (2008, Figs. 2 and 3).

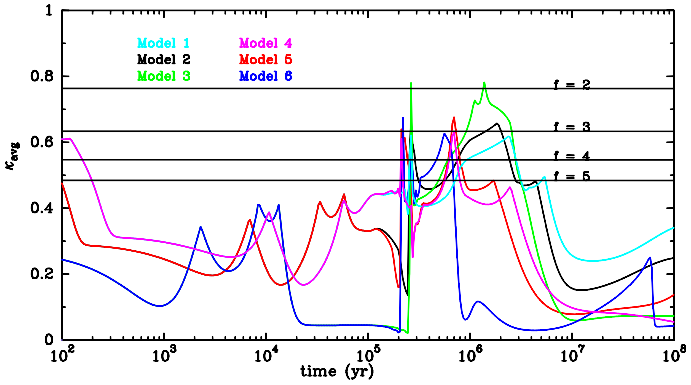

Fig. 6. Mean confidence level κ_{avg} calculated for the chemical models as explained in the text (Garrod et al. 2007).

Ion-molecule chemistry forms a relatively large abundance of this species at early times, followed by a depletion to grain surfaces. This depletion happens at slightly earlier times for models with larger values of density. Although C_3 is frozen on the dust grains, it is not liberated directly from the grains during the warm-up, but rather is produced in a reaction sequence starting with CH_4. The C_3(s) however is more likely to participate in surface reactions than to desorb. The reaction of C + C_2H_2 produces C_3 through reaction (19). This mechanism and the secondary pathways result in the formation of a peak in the abundance during and after the warm-up period. The formation of c-C_3H_2 can proceed via three pathways. The first mechanism is reaction (21), in which C_3H_3 reacts with H. The dissociative recombination of $C_3H_3^+$ (22) is a second mechanism. Alternatively, reaction (23) of CH with C_2H_2 is another important formation pathway.

4.4. Best fit chemical model

In order to compare model results with observations on a more quantitative basis, we compute the mean confidence level (Garrod et al. 2007) during the warm-up period. In this quasi-statistical analysis introduced by Garrod et al. (2007), the confidence level, κ_i, for agreement between computed and observed abundances is defined as

$$\kappa_i = erfc\left(\frac{|\log(X_i) - \log(X_{obs,i})|}{\sqrt{(2)}\sigma}\right). \quad (1)$$

Table 9. Dominant reactions of observed and intermediate species following CH_4 sublimation.

			C_2H_2:				
1.)	C^+	+	CH_4	→	$C_2H_3^+$	+	H
2.)	$C_2H_3^+$	+	e	→	C_2H_2	+	H
3.)	C^+	+	CH_4	→	$C_2H_2^+$	+	H_2
4.)	$C_2H_2^+$	+	H_2	→	$C_2H_4^+$		
5.)	$C_2H_4^+$	+	e	→	C_2H_2	+	2 H
			C_3H_3:				
6.)	$C_2H_3^+$	+	CH_4	→	$C_3H_5^+$	+	H_2
7.)	$C_2H_2^+$	+	CH_4	→	$C_3H_5^+$	+	H
8.)	$C_3H_5^+$	+	e	→	C_3H_3	+	H_2
			$C_3H_3^+$:				
9.)	C	+	C_2H_2	→	C_3H	+	H
10.)	HCO^+	+	C_3	→	C_3H^+	+	CO
11.)	C^+	+	C_2H_2	→	C_3H^+	+	H
12.)	HCO^+	+	C_3H	→	$C_3H_2^+$	+	CO
13.)	C_3H^+	+	H_2	→	$C_3H_2^+$	+	H
14.)	$C_3H_2^+$	+	CH_4	→	$C_3H_3^+$	+	CH_3
15.)	HCO^+	+	c-C_3H_2	→	$C_3H_3^+$	+	CO
16.)	C_3H^+	+	H_2	→	$C_3H_3^+$		
			CCH:				
17.)	$C_2H_3^+$	+	e	→	**CCH**	+	2 H
18.)	HCO^+	+	**CCH**	→	$C_2H_2^+$	+	CO
			C_3:				
19.)	C	+	C_2H_2	→	**C_3**	+	H_2
20.)	**CCH**	+	**C_3**	→	C_5	+	H
			c-C_3H_2:				
21.)	H	+	C_3H_3	→	c-C_3H_2	+	H_2
22.)	$C_3H_3^+$	+	e	→	**c-C_3H_2**	+	H
23.)	CH	+	C_2H_2	→	c-C_3H_2	+	H
24.)	HCO^+	+	c-C_3H_2	→	$C_3H_3^+$	+	CO

Notes. The observed species are identified in bold type.

The index i refers to individual chemical species under consideration. The mean of the individual values of κ_i thus computed is denoted by κ_{avg}. Since we consider the computed abundance to "fit" the observation if the abundance agrees within an order of magnitude or better we assume $\sigma = 1$ so that one standard deviation corresponds to agreement of one order of magnitude. The related confidence level for such a factor of 10 agreement is $\kappa_i = 0.317$, and the value increases up to $\kappa_i = 1$ for closer

agreement. The accuracy of this analysis and the robustness of κ_{avg} against individual values of κ_i improve with increasing size of the considered dataset. Since we have considered only three chemical species, we use the κ-based analysis primarily as a guideline to identify models that best reproduce the data. The best fit corresponds to the maximum average confidence level.

Figure 6 shows the κ_{avg} values for each model that we have considered here, along with horizontal lines indicating agreement within a factor (f) of 2, 3, 4, and 5. The primary interpretation of this diagram is that all six models reasonably fit the observed abundances during the period following the warm-up. Models 1–3 fit the observation set within a factor of 2–4 or better for the time period of $t \sim 0.7$–3 Myr for all three density values. Models 4–6 fit the observation set within a factor of 3–5 or better for the period of $t \sim 0.6$–0.8 Myr for models 4 and 5 and for the earlier period $t \sim 0.3$–0.7 Myr for model 6. Model 3 gives the best agreement with observations in terms of the value and duration of the κ_{avg} function, while model 2 is the second best at meeting these criteria. This analysis quantitatively asserts the level of model agreement described in Fig. 5 and broadly shows that the best sustained agreement of the models occurs in the time following the warm-up, rather than earlier or later.

5. Discussion

5.1. Lower gas phase abundance of C_3 in MM1

The angular resolution of the spectroscopic observations used in this paper lies between 12 and 40″, so that MM1 and MM2, are not resolved spatially. However, due to their markedly different velocities, MM1, MM2, and the envelope are easily discernible in the spectra. Interestingly, all C_3 spectra show primarily two velocity components associated with MM2 and the envelope, with absorption due to MM1 being detected only in $Q(4)$. In contrast, the chemically related species CCH and c-C_3H_2 that we have considered here show components corresponding to only MM1 and the envelope. Thus, there is an intrinsic difference in the distribution of C_3 compared to the distribution of the other species. The abundance of C_3 in MM2 (1.2×10^{-9}) is only twice that in the envelope (6.3×10^{-10}). Based on Table 1, the total column density of MM1 is ∼60% of the column density of MM2. This suggests that if the relative abundances of C_3 in MM1 and MM2 were similar, the total column density of C_3 in MM1 would have been 2.5 times the column density in the envelope so that the absorption dips due to MM1 would be similar to or stronger than the dip due to the envelope. It may be argued that the continuum backgrounds for the two components MM1 and the envelope may be different. However the continuum from MM1 is expected to be stronger than the continuum from the envelope. All these arguments indicate that C_3 is preferentially depleted or destroyed in MM1.

One major difference between MM1 and MM2 lies in the fact that MM1 has already shown evidence for at least one high temperature hot core, whereas MM2, though more massive, shows no such components. The chemical network includes among others the reaction $C_3 + H_2 \rightarrow C_3H + H$ (Pineau des Forêts et al. 1988), which becomes a primary destruction pathway for C_3 when the temperature exceeds ≈80 K. As a result, models predict that C_3 will be depleted in favor of c-C_3H_2 in hot core conditions, as C_3H is also destroyed by reaction with H_2. Additionally, the chemical models presented here also show that the C_3 abundance is reduced at larger densities. MM1 is definitely at a higher density than the envelope (Table 1), so that the reduced abundance of C_3 in MM1 relative to MM2 could also indicate that MM2 has a density lower than MM1. We note that this contradicts the densities derived from dust column densities (Table 1), which is not completely unexpected since the densities derived from the column densities are beam averaged and need not always reflect the local densities in a region.

However, an alternate possibility arises from the fact that the source intrinsic continuum opacity can refill the absorption to a significant extent, so that the column densities derived here are all primarily lower limits (Mookerjea et al. 2010). It can thus be envisaged that in the case of MM1, which has a stronger continuum emission, it is a combination of the geometry of the source and the refilling of the absorption dip that reduces the "visibility" of C_3. A proper evaluation of the effect of the continuum opacity on the absorption depth is possible only by constructing a complete radiative transfer model of the entire region with accurate temperature and density profiles, which are not yet available.

Finally, since MM2 is estimated to be younger than MM1 and c-C_3H_2, and CCH emission from MM2 are not detected, the possibility that the observed C_3 abundance in MM2 is due to the pre-warm-up gas-phase chemistry can also not be ruled out.

5.2. Comparison with C_3 in diffuse clouds

In diffuse clouds C_3 has been found to have an almost one-to-one correlation with C_2 (Roueff et al. 2002). In addition, the abundance of C_3 in diffuse clouds, $(3–6)\times10^{-9}$ (Roueff et al. 2002), is ten times larger than the abundance of C_3 derived in the dense star-forming environment of DR21(OH). Oka et al. (2003) had explained the observed correlation between C_2 and C_3 in diffuse clouds in terms of a direct pathway of formation of C_3 from C_2 (see their Fig. 4). In the previous section, we examined the formation of C_3 during a warm-up period and noted a relatively larger abundance of this species prior to $t = 10^5$ yr, the so-called "early time". We now explore the chemistry of C_3 in diffuse regions and during the early time period in dense gas regions in order to examine the differences (if any).

The first step of the transformation of C_2 to C_3 in diffuse clouds is the photoionization of C_2 to C_2^+ (Oka et al. 2003). In contrast, the models for the dense star-forming regions assume darker ($A_V = 10$) conditions, so photoionization is not an effective process.

In dense models, the process begins with the radiative association of $C^+ + H_2 \rightarrow CH_2^+$. Next, CH_2^+ reacts with H_2 to form CH_3^+. This is followed by the dissociative recombination of CH_3^+ and CH_2^+ as competitive reactions to form CH and then by an ion-neutral reaction with C^+ to form C_2^+. As shown in Fig. 4 of (Oka et al. 2003), the pathway subsequently follows along the upper (C_2H) branch to form C_3. The C_3 is destroyed by processes that form C_4, C_4^+, and C_5, which react further to primarily form C_3 in a cyclic process. The abundance of C_3 grows until C^+ is depleted at $t \sim$ 10–100 yr, depending on the density, after which it reaches a plateau until the C_3 is accreted onto grain surfaces. Dissociative recombination reactions with C_2H^+, $C_2H_2^+$, and C_3^+ along the pathway form C_2. The C_2 then reacts with O to form CO, and the abundance consequently falls to $X(C_2) \sim 10^{-9}$, far below the $X(C_2)$:$X(C_3) = 40 : 1$ measured by Oka et al. (2003) for diffuse clouds.

Thus, C_2 is not the starting point for C_3 formation in dense cloud models at early times and does not undergo a cycling process like that of C_3. As a result, the correlation between C_2 and C_3 abundance is not predicted by dark cloud models. Rather, the C_2 abundance evolution more closely follows the evolution of CCH from early times until the warm-up begins than that of C_3. This comparison indicates that the chemistry of C_3 formation in

the envelope of DR21(OH) is definitely not the same as in diffuse clouds. Furthermore, the early time abundance of C_3 for dense regions exceeds the observed abundance by three orders of magnitude, effectively excluding this formation route as well.

5.3. Warm carbon chain chemistry in the envelope

Comparison of the present model results and observations indicates that the observed composition can be simulated with ion-molecule chemistry following a moderate warm-up to 30–50 K. This also means that C_3 formation in star-forming regions can be explained in terms of the moderate temperature (30 K) gas-phase chemical reactions starting from CH_4 evaporated from the grain mantle only and thus does not require photochemistry of PAH molecules.

The observed abundances of C_3 are consistent with formation during a warm-up model, "warm carbon chain chemistry" (WCCC; Sakai et al. 2008), and are related to the abundances of CCH, c-C_3H_2. This suggests that the envelope conditions are more like those of "lukewarm corinos" surrounding low-mass protostars than those of hot cores. In other words, the C_3 is not residing in a hot core. The abundances of the additional species chemically related to C_3, which we consider for the case of DR21(OH), provided further insight regarding the envelope conditions.

Table 6 summarizes the observed abundances of the different species in DR21(OH) as well as those available in the literature for two types of sources: the lukewarm corinos L1527 and B228 and the hot corino IRAS 16293-2422. We find that while C_3 has not been observed in any of the other sources, the abundances of the other three species in DR21(OH) are closer to the abundances observed in lukewarm corinos. In addition, the chemical model that best represents the observed abundances corresponds to a $T_{\rm max}$ of 30–50 K, a temperature that is much lower than the values expected in hot cores/corinos. This suggests that the envelope of DR21(OH) is chemically closer to a WCCC region such as a lukewarm corino envelope than to a hot core. Furthermore, the predepletion C_3 abundance (at $t \leq 10^4$ yr) exceeds the observed values by a large factor. This implies that the C_3 abundance is primarily maintained via ion-molecule chemistry in the gas phase after CH_4 is desorbed from the surface of the dust grains and does not have a one-to-one correlation with C_2 as found in diffuse clouds.

5.4. Chemical and dynamical ages of the region

The chemistry of the envelope surrounding the embedded sources MM1 and MM2 in DR21(OH) appears to have occurred over a period between (0.7–3) Myr, including a cold period, warm-up, and extended time at $T = 30$ or 50 K. This time period seems to be on the longer side of the evolutionary timescales of massive star-forming cores. As detailed by Csengeri et al. (2011), the lifetime of the gas in massive dense cores is determined by the crossing times or the local free-fall times for the molecular dense cores which is $(5–7) \times 10^4$ yr. However, the large-scale flows associated with Cygnus X (and DR21 in particular) are massive enough to continuously replenish the mass of these cores, allowing them to remain "active" for a much longer period of time. In addition, the dynamical time of the most massive sub-filament in DR21 is ~2 Myr (Schneider et al. 2010). Thus, the chemical age of ~1 Myr is consistent with the dynamical age of the region.

6. Summary

Using the high-velocity resolution of HIFI, in the DR21(OH) region, we detect absorption due to C_3 from the envelope and the less evolved core (MM2) as well as a rather weak signal associated to the most massive and hottest region (MM1). The abundance of C_3 in the envelope of the hot core associated with DR21(OH) has been consistently explained along with those of other species formed in the same chemical network using a chemical model involving the warm-up of grains. The formation mechanism of C_3 required to explain the observed abundances in dense star-forming regions is the gas-phase reaction of CH_4 desorbed from the grain surfaces that have been warmed up. It is neither formed in a cycle with C_2 as the starting point nor produced by the photodestruction cascades of PAH molecules. For the envelope of DR21(OH), the chemical models that best explain the abundances of C_3 and other chemically related species correspond to models 2 and 3, $n_{\rm H_2} = 1–5 \times 10^6$ cm^{-3} for $T_{\rm max} = 30$ K , for a time period between 0.7–3 Myr and model 6, $n_{\rm H_2} = 5 \times 10^6$ cm^{-3} for $T_{\rm max} = 50$ K, for a time period between 0.6–0.8 Myr. The upper limit of the timescale, though much larger than the typical lifetimes of hot (warm) cores, is not unrealistic in the case of DR21(OH), where the dynamic age of the most massive filament has been estimated to be 2 Myr.

Acknowledgements. HIFI has been designed and built by a consortium of institutes and university departments from across Europe, Canada and the United States under the leadership of SRON Netherlands Institute for Space Research, Groningen, The Netherlands and with major contributions from Germany, France and the US. Consortium members are: Canada: CSA, U. Waterloo; France: CESR, LAB, LERMA, IRAM; Germany: KOSMA, MPIfR, MPS; Ireland, NUI Maynooth; Italy: ASI, IFSI-INAF, Osservatorio Astrofisico di Arcetri-INAF; The Netherlands: SRON, TUD; Poland: CAMK, CBK; Spain: Observatorio Astronómico Nacional (IGN), Centro de Astrobiologá (CSIC-INTA). Sweden: Chalmers University of Technology – MC2, RSS & GARD; Onsala Space Observatory; Swedish National Space Board, Stockholm University – Stockholm Observatory; Switzerland: ETH Zurich, FHNW; USA: Caltech, JPL, NHSC. B.M. acknowledges the support from the Alexander von Humboldt Foundation. M.G. acknowledges the support received from CNES. J.R.G. and J.C. thank the Spanish MICINN for funding support through grants, AYA2009-07304 and CSD2009-00038. J.R.G. is supported by a Ramòn y Cajal research contract M.S. acknowledges support from grant No. 203 393334 from Polish MNiSW. E.H. thanks NASA for partial support of this work through the *Herschel* program, administered by the Jet Propulsion Laboratory. This work was carried out in part at the Jet Propulsion Laboratory, California Institute of Technology, which is supported by NASA. T.C.'s contribution was funded by ERC Advanced Investigator Grant GLOSTAR (247078). This paper has made extensive use of the SIMBAD database, operated at CDS, Strasbourg, France. This research made use of the myXCLASS program (https://www.astro.uni-koeln.de/projects/schilke/XCLASS), which accesses the CDMS (http://www.cdms.de) and JPL (http://spec.jpl.nasa.gov) molecular data bases.

References

Ádámkovics, M., Blake, G. A., & McCall, B. J. 2003, ApJ, 595, 235
Aikawa, Y., Wakelam, V., Garrod, R. T., & Herbst, E. 2008, ApJ, 674, 984
Araya, E. D., Kurtz, S., Hofner, P., & Linz, H. 2009, ApJ, 698, 1321
Argon, A. L., Reid, M. J., & Menten, K. M. 2000, ApJS, 129, 159
Bernst, I., Schilke, P., Moeller, T., et al. 2011, Astronomical Data Analysis Software and Systems XX, 442, 505
Beuther, H., Semenov, D., Henning, T., & Linz, H. 2008, ApJ, 675, L33
Bisschop, S. E., Jørgensen, J. K., van Dishoeck, E. F., & de Wachter, E. B. M. 2007, A&A, 465, 913
Cazaux, S., Tielens, A. G. G. M., Ceccarelli, C., et al. 2003, ApJ, 593, L51
Cernicharo, J., Goicoechea, J. R., & Caux, E. 2000, ApJ, 534, L199
Chandler, C. J., Moore, T. J. T., Mountain, C. M., & Yamashita, T. 1993, MNRAS, 261, 694
Comito, C., Schilke, P., Phillips, T. G., et al. 2005, ApJS, 156, 127
Csengeri, T., Bontemps, S., Schneider, N., et al. 2011, ApJ, 740, L5
Fish, V. L., Reid, M. J., Argon, A. L., & Zheng, X.-W. 2005, ApJS, 160, 220
de Graauw, T., Helmich, F. P., Phillips, T. G., et al. 2010, A&A, 518, L6
Galazutdinov, G., Pětlewski, A., Musaev, F., et al. 2002, A&A, 395, 969

Garrod, R. T., & Herbst, E. 2006, A&A, 457, 927
Garrod, R. T., Wakelam, V., & Herbst, E. 2007, A&A, 467, 1103
Gendriesch, R., Pehl, T. F., Winnewisser, G., et al. 2003, Z. Naturforsch., 58a, 129
Gerin, M., De Luca, M., Black, J., et al. 2010, A&A, 518, L110
Gerin, M., Kaźmierczak, M., Jastrzebska, M., et al. 2011, A&A, 525, A116
Giesen, T. F., Van Orden, A. O., Cruzan, J. D., et al. 2001, ApJ, 551, L181
Haffner, L. M., & Meyer, D. M. 1995, ApJ, 453, 450
Hasegawa, T. I., Herbst, E., & Leung, C. M. 1992, ApJS, 82, 167
Hassel, G. E., Herbst, E., & Garrod, R. T. 2008, ApJ, 681, 1385
Hassel, G. E., Harada, N., & Herbst, E. 2011, ApJ, 743, 182
Hinkle, K. W., Keady, J. J., & Bernath, P. F. 1988, Science, 241, 1319
Maier, J. P., Lakin, N. M., Walker, G. A. H., et al. 2001, ApJ, 553, 267
Mangum, J. G., Wootten, A., & Mundy, L. G. 1991, ApJ, 378, 576
Mangum, J. G., Wootten, A., & Mundy, L. G. 1992, ApJ, 388, 467
Mauersberger, R., Henkel, C., Wilson, T. L., & Walmsley, C. M. 1986, A&A, 162, 199
Mookerjea, B., Giesen, T., Stutzki, J., et al. 2010, A&A, 521, L13
Motte, F., Bontemps, S., Schilke, P., et al. 2007, A&A, 476, 1243
Müller, H. S. P., Schlöder, F., Stutzki, J., & Winnewisser, G. 2005, J. Mol. Struct., 742, 215
Öberg, K. I., Fuchs, G. W., Awad, Z., et al. 2007, ApJ, 662, L23
Öberg, K. I., Linnartz, H., Visser, R., & van Dishoeck, E. F. 2009a, ApJ, 693, 1209
Öberg, K. I., van Dishoeck, E. F., & Linnartz, H. 2009b, A&A, 496, 281
Oka, T., Thorburn, J. A., McCall, B. J., et al. 2003, ApJ, 582, 823
Ott S. 2010, in Astronomical Data analysis Software and Systems XIX, eds. Y. Mizumoto, K. I. Morita, & M. Ohishi, ASP Conf. Ser., in press
Pety, J., Teyssier, D., Fossé, D., et al. 2005, A&A, 435, 885
Pilbratt, G. L., Riedinger, J. R., Passvogel, T., et al. 2010, A&A, 518, L1
Pineau des Forêts, G., Flower, D. R., & Dalgarno, A. 1988, MNRAS, 235, 621
Plambeck, R. L., & Menten, K. M. 1990, ApJ, 364, 555
Radi, P. P., Bunn, T. L., Kemper, P. R., Molchan, M. E., & Bowers, M. T. 1988, J. Chem. Phys., 88, 2809
Reipurth, B., & Schneider, N. 2008, Handbook of Star Forming Regions, Vol. I, 36
Richardson, K. J., Sandell, G., Cunningham, C. T., & Davies, S. R. 1994, A&A, 286, 555
Roelfsema, P. R., Helmich, F. P., Teyssier, D., et al. 2012, A&A, 537, A17
Roueff, E., Felenbok, P., Black, J. H., & Gry, C. 2002, A&A, 384, 629
Rygl, K. L. J., Brunthaler, A., Sanna, A., et al. 2012, A&A, 539, A79
Sakai, N., Sakai, T., Hirota, T., & Yamamoto, S. 2008, ApJ, 672, 371
Sakai, N., Sakai, T., Hirota, T., Burton, M., & Yamamoto, S. 2009a, ApJ, 697, 769
Sakai, N., Sakai, T., Hirota, T., & Yamamoto, S. 2009b, ApJ, 702, 1025
Schilke, P., Phillips, T. G., & Mehringer, D. M. 1999, The Physics and Chemistry of the Interstellar Medium, 330
Schmuttenmaer, C. A., Cohen, R. C., Pugliano, N., Heath, J. R., & Cooksy, A. L. 1990, Science, 249, 897
Schneider, N., Csengeri, T., Bontemps, S., et al. 2010, A&A, 520, A49
Van Orden, A., Cruzan, J. D., Provencal, R. A., et al. 1995, in Proc. Airborne Astronomy Symp. on the Galactic Ecosystem, eds. M. R. Haas, J. A. Davidson, & E. F. Erickson (San Francisco: ASP), ASP Conf. Ser., 73, 67
White, G. J., Abergel, A., Spencer, L., et al. 2010, A&A, 518, L114
Wilson, T. L., & Mauersberger, R. 1990, A&A, 239, 305
Zapata, L. A., Loinard, L., Su, Y.-N., et al. 2012, ApJ, 744, 86